

# Accepted Manuscript

Water-exchange MRI detects subtle blood-brain barrier breakdown in Alzheimer's disease rats

Ben R. Dickie, Matthias Vandesquille, José Ulloa, Hervé Boutin, Laura M. Parkes, Geoff.J.M. Parker



PII: S1053-8119(18)30815-2

DOI: [10.1016/j.neuroimage.2018.09.030](https://doi.org/10.1016/j.neuroimage.2018.09.030)

Reference: YNIMG 15266

To appear in: *NeuroImage*

Received Date: 24 May 2018

Revised Date: 5 September 2018

Accepted Date: 12 September 2018

Please cite this article as: Dickie, B.R., Vandesquille, M., Ulloa, José., Boutin, Hervé., Parkes, L.M., Parker, G.J.M., Water-exchange MRI detects subtle blood-brain barrier breakdown in Alzheimer's disease rats, *NeuroImage* (2018), doi: <https://doi.org/10.1016/j.neuroimage.2018.09.030>.

This is a PDF file of an unedited manuscript that has been accepted for publication. As a service to our customers we are providing this early version of the manuscript. The manuscript will undergo copyediting, typesetting, and review of the resulting proof before it is published in its final form. Please note that during the production process errors may be discovered which could affect the content, and all legal disclaimers that apply to the journal pertain.

1 **Title:**

2 Water-exchange MRI detects subtle blood-brain barrier breakdown in Alzheimer's disease rats

3 **Author names and affiliations:**4 Ben R. Dickie<sup>1</sup>, Matthias Vandesquille<sup>1</sup>, José Ulloa<sup>2</sup>, Hervé Boutin<sup>1</sup>, Laura M. Parkes<sup>1,+</sup>, Geoff J. M.  
5 Parker<sup>1,2,+</sup>6 1. Division of Neuroscience and Experimental Psychology, Faculty of Biology, Medicine, and Health,  
7 Stopford Building, University of Manchester, UK

8 2. Bioxydyn Ltd, Manchester, UK

9 <sup>+</sup>Joint senior authors10 **Corresponding author:**11 [Ben.dickie@manchester.ac.uk](mailto:Ben.dickie@manchester.ac.uk)12 **Present address:**13 Room G724a  
14 Stopford Building  
15 99 Oxford Road  
16 The University of Manchester  
17 M13 9PG18 **Abstract**19  
20  
21 Blood-brain barrier (BBB) breakdown has been hypothesized to play a key role in the onset and  
22 progression of Alzheimer's disease (AD). However, the question of whether AD itself contributes to  
23 loss of BBB integrity is still uncertain, as many *in-vivo* studies have failed to detect signs of AD-related  
24 BBB breakdown. We hypothesize AD-related BBB damage is subtle, and that these negative results  
25 arise from a lack of measurement sensitivity. With the aim of developing a more sensitive measure of  
26 BBB breakdown, we have designed a novel MRI scanning protocol to quantify the trans-BBB  
27 exchange of endogenous water. Using this method, we detect increased BBB water permeability in a  
28 rat model of AD that is associated with reduced expression of the tight junction protein occludin. BBB  
29 permeability to MRI contrast agent, assessed using dynamic contrast-enhanced (DCE)-MRI, did not  
30 differ between transgenic and wild-type animals and was uncorrelated with occludin expression. Our  
31 data supports the occurrence of AD-related BBB breakdown, and indicates that such BBB pathology  
32 is subtle and may be undetectable using existing 'tracer leakage' methods. Our validated water-  
33 exchange MRI method provides a new powerful tool with which to study BBB damage *in-vivo*.34 **Keywords:** water-exchange, MRI, blood-brain barrier, Alzheimer's, permeability surface-area product,  
35 cerebrovascular dysfunction

36

37

38

39

40

41

42

## 43 1.1 Introduction

44 Loss of blood-brain barrier (BBB) integrity occurs in ageing (Farrall and Wardlaw, 2009; Montagne et  
 45 al., 2016), and has been hypothesized to play a key role in the onset of Alzheimer's disease (AD)  
 46 (Zlokovic, 2011). Growing evidence suggests BBB breakdown may occur when amyloid- $\beta$  ( $A\beta$ )  
 47 peptides interact with blood vessels in the brain, a process which causes arteriolar and capillary  
 48 amyloid angiopathy (CAA) (Weller et al., 2008) and reduces the expression of BBB tight-junction  
 49 proteins that maintain paracellular BBB integrity (Carrano et al., 2011; Keaney et al., 2015; Kook et  
 50 al., 2012). Patients with AD typically have more severe CAA than age-matched non-AD patients  
 51 (Vinters, 1987), which potentially exacerbates age-related cerebrovascular damage (Dorr et al., 2012)  
 52 and alters  $A\beta$  clearance from the brain (Weller et al., 2008). However, the question of whether AD  
 53 itself reduces BBB integrity remains unresolved, due to a number of conflicting studies (Bien-Ly et al.,  
 54 2015; Caserta et al., 1998; Farrall and Wardlaw, 2009; Montagne et al., 2015; Schlageter et al., 1987;  
 55 Starr et al., 2009; van de Haar et al., 2014; Wang et al., 1998)

56 Current methods for probing BBB integrity *in-vivo* monitor and detect the leakage of injectable small-  
 57 molecular weight probes as they passively diffuse from blood to brain. However, in the case of an  
 58 intact BBB or subtle BBB breakdown, leakage of these probes into tissue is slow, resulting in the need  
 59 for long measurement durations to resolve differences in leakage between study groups (Armitage et  
 60 al., 2011; Heye et al., 2016). Based on the known sensitivity of magnetic resonance imaging (MRI) to  
 61 compartmental water exchange (Bains et al., 2010; Donahue et al., 1997; Landis et al., 1999), we  
 62 have developed an MRI technique for detection of subtle BBB breakdown, based on measuring the  
 63 trans-BBB transport of endogenous water. Specifically, we use an MRI contrast agent to shorten the  
 64 spin-lattice relaxation time of blood, which increases the impact of trans-BBB water-exchange on MRI  
 65 signals and makes possible the estimation of mean blood water residence time ( $\tau_b$ ) simultaneously  
 66 with the blood water population fraction ( $p_b$ ). The ratio of these measurements provides the trans-BBB  
 67 permeability surface-area product to water ( $PS_w$ ), a quantity we hypothesize to be more sensitive to  
 68 subtle BBB breakdown compared to existing 'tracer leakage' measurements.

69 We first undertake sensitivity analyses and simulations to determine the optimal acquisition  
 70 parameters for our water-exchange technique and to assess possible sources of bias in parameter  
 71 estimates. The optimised MRI protocol, termed multi-flip angle multi-echo (MFAME)-MRI, is then used  
 72 to measure BBB  $PS_w$  in a rat model of early-onset AD (TgF344-AD), alongside measures of contrast  
 73 agent leakage rate,  $K^{trans}$ . Transgenic rats display increased  $PS_w$  relative to wild-type littermates, but  
 74 BBB permeability to contrast agent remains unchanged. To understand the potential cause of  
 75 increased  $PS_w$ , we then undertook immunostaining of tight junction proteins and show that  $PS_w$   
 76 correlates inversely with the expression of occludin at the BBB.

## 77 1.2 Material and methods

### 78 1.2.1 Sensitivity analysis

79 The change in spoiled gradient echo (SPGR) MRI signal,  $\Delta S$ , due to unit changes in  $p_b$ ,  $\tau_b$  and  $PS_w$   
 80 was simulated using the SPGR-2S1X model (equations 3-6 to be found in section 1.2.5) for flip angles  
 81 between 0-90 degrees, repetition times between 0-400 ms, and blood contrast agent concentrations  
 82 ( $C_b$ ) between 0-10 mM. A unit change was defined as a 50% increase in the parameter of interest.  
 83 When varying flip angle, a TR = 100 ms and  $C_b = 4.8$  mM was used. When varying TR, a flip angle =  
 84  $30^\circ$  and  $C_b = 4.8$  mM was used. When varying  $C_b$ , a TR = 100 ms and a flip angle =  $40^\circ$  were used. A  
 85 single set of representative tissue parameters were taken from the literature (Schwarzbauer et al.,  
 86 1997; Zhang et al., 2013). Assuming 7T MRI these were:  $T_{1e} = 1.8$  s,  $T_{1b} = 2.1$  s,  $p_b = 0.020$  mL mL<sup>-1</sup>,  
 87  $\Delta p_b = 0.010$  mL mL<sup>-1</sup>,  $\tau_b = 0.40$  s,  $\Delta \tau_b = 0.20$  s and  $PS_w = 3.0$  mL min<sup>-1</sup> mL<sup>-1</sup>,  $\Delta PS_w = 1.5$  mL min<sup>-1</sup>  
 88 mL<sup>-1</sup>. Plots of  $\Delta S/\Delta p_b$ ,  $\Delta S/\Delta \tau_b$ , and  $\Delta S/\Delta PS_w$  versus flip angle, TR, and  $C_b$  were generated to  
 89 determine the optimal acquisition parameters. Parameter definitions are given in section 1.2.5.

## 90 1.2.2 Monte Carlo Simulations

91 To estimate  $PS_w$ , the separate effects of  $p_b$  and  $\tau_b$  on MRI signals must be distinguished. This requires  
 92 acquisition of a minimum of 2 images with different flip angles or TRs, assuming all other model  
 93 parameters are known. In this study we opt to acquire 5 flip angles while using a relatively long TR  
 94 (100 ms). This protocol was chosen as opposed to using multiple TRs to provide an invariant and  
 95 sufficient time delay between each RF pulse to acquire a multi-gradient echo readout for  $T_2^*$  decay  
 96 correction.

97 To determine the optimal use of imaging time, Monte Carlo simulations were performed to assess  
 98 how the precision of  $p_b$  and  $\tau_b$  estimates depend on the number of distinct post-contrast flip angles  
 99 and image repetitions. Simulations were undertaken under the following conditions: 3 flip angles and  
 100 10 repeats (resulting in a total of 30 images), 4 flip angles and 7 or 8 repeats (also 30 images), and 5  
 101 flip angles and 6 repeats (also 30 images). For each simulation, flip angles were equally spaced  
 102 across the range  $10^\circ$ -  $80^\circ$ . Each fit was repeated 100 times in a Monte Carlo simulation using a range  
 103 of zero mean Gaussian noise levels (noise standard deviation/ $S_0 = 0.00001$  to  $0.004$ ). Relative  
 104 precision in parameter estimates was quantified using the coefficient of variation (CoV):

$$CoV = \frac{IQR(\hat{x})}{median(\hat{x})} \quad (1)$$

105

106 where IQR is the inter-quartile range, and  $\hat{x}$  is the parameter estimate.

107 Next, we assessed the effect of transmit  $B_1$  field ( $B_1^+$ ) inhomogeneity and non-zero trans-BBB contrast  
 108 agent leakage on SPGR-2S1X parameter estimates. Synthetic multiple-flip angle images ( $\alpha = 10^\circ$ ,  
 109  $20^\circ$ ,  $40^\circ$ , and  $60^\circ$  at a TR = 100 ms) were simulated for estimation of pre-contrast  $T_{1b}$  and  $T_{1t}$ .  
 110 Dynamic SPGR images ( $\alpha = 60^\circ$ , TR = 20 ms) were generated to track  $C_b(t)$  during a simulated  
 111 injection of contrast agent. A population average  $C_b(t)$  measured from the TgF344-AD rats was used.  
 112 For estimation of  $p_b$  and  $\tau_b$ , multiple flip angle images at 5 distinct flip angles ( $\alpha = 10^\circ$ ,  $20^\circ$ ,  $30^\circ$ ,  $40^\circ$ ,  
 113 and  $80^\circ$ ) were simulated. All images were created as  $10 \times 10$  grids, giving 100 voxels in total.

114 To assess the effect of  $B_1^+$  inhomogeneity on parameter estimates, images were generated across a  
 115 range of realistic flip angle errors ( $\pm 10\%$ ). Parameters  $p_b$ ,  $\tau_b$ , and pre-contrast  $T_{1e}$  and  $T_{1b}$ , were set to  
 116  $0.02 \text{ mL mL}^{-1}$ ,  $0.4 \text{ s}$ ,  $1.8 \text{ s}$  and  $2.1 \text{ s}$ , respectively (Schwarzbauer et al., 1997; Zhang et al., 2013).  
 117 Contrast agent  $T_1$  relaxivity ( $r_1$ ) was assumed to be  $3.5 \text{ (mM s)}^{-1}$  for both blood and tissue. Equation 1  
 118 was then fitted back to the simulated data assuming accurate flip angles. Relative bias of each  
 119 parameter was estimated as:

$$\lambda = \frac{median(\hat{x}) - x}{x} \quad (2)$$

120

121

122 where  $\hat{x}$  is the parameter estimate and  $x$  is the true parameter value (ground truth).

123 In an attempt to correct observed biases in parameter estimates due to  $B_1^+$  inhomogeneity, an  
 124 additional set of pre-contrast multi-flip angle images with a long TR were simulated ( $\alpha = 5^\circ$ ,  $10^\circ$ ,  $20^\circ$ ,  
 125  $30^\circ$ ,  $40^\circ$ ,  $60^\circ$ ,  $80^\circ$ ,  $90^\circ$ , TR = 5000 ms). Varying the TR of SPGR images alters the  $T_1$  and  $B_1^+$   
 126 weighting (Voigt et al., 2010; Yarnykh, 2007). Thus, by jointly fitting SPGR signal models to long and  
 127 short TR multi-flip angle images, we aim to remove the effects of  $B_1^+$  inhomogeneity on estimates of  
 128  $T_1$ , and importantly  $PS_w$ . Simulations described above were repeated with the proposed flip angle  
 129 correction method, and the bias in estimated parameters computed.

130 To simulate leakage of contrast agent across the BBB,  $T_{1e}$  was allowed to decrease in response to an  
 131 increasing extravascular contrast agent concentration,  $C_e(t)$ .  $C_e(t)$  was calculated from the two-  
 132 compartment exchange model (Brix et al., 2004) using the population-based estimate of  $C_b(t)$  and  
 133  $K^{trans}$  in the range  $10^{-5} - 10^{-3} \text{ min}^{-1}$ . Signal models (Eqn 3.) were then fit back to the simulated data  
 134 assuming  $K^{trans} = 0 \text{ min}^{-1}$ , and the bias in  $p_b$ ,  $\tau_b$ , and  $PS_w$  computed.

### 135 1.2.3 Animals

136 Male only TgF344-AD ( $n = 7$ ) and wild-type (WT) littermates ( $n = 5$ ) aged 18.3 months (range 17.9 -  
 137 18.8 months) were scanned using the MFAME-MRI protocol (see section 1.2.4 for details), then culled  
 138 for immunohistochemistry. This rat model of AD has previously been shown to display widespread A $\beta$   
 139 deposition in the form of plaques and cerebral amyloid angiopathy (Cohen et al., 2013) and to have  
 140 early neurovascular dysfunction (Joo et al., 2017). All scanning was performed between the hours of  
 141 10.00am and 4.00pm across 9 days spanning a 2 month period. The time between scanning and  
 142 culling was  $4.6 \pm 2.3$  weeks (mean  $\pm$  sd). All experimental procedures were approved by the  
 143 Preclinical Imaging Executive Committee of the University of Manchester and carried out in  
 144 accordance with the U.K Animals (Scientific Procedures) Act 1986 and EU Directive 2010/63/EU for  
 145 animal experiments. Breeding, housing, and husbandry details, conforming to the ARRIVE guidelines  
 146 (Kilkenny et al., 2010) can be found in supplementary materials.

### 147 1.2.4 MRI protocol

148 All rats were initially anesthetised with 4% isoflurane + 100%  $O_2$  then maintained with 2-2.5%  
 149 isoflurane + 100%  $O_2$  for the duration of scanning. Scans were acquired on a Bruker Avance III  
 150 console interfaced with an Agilent 7T 16cm bore magnet. A Bruker transmit only resonator  
 151 (T11070V3) was used for transmission and a Bruker rat brain surface coil (T11205V3) was used for  
 152 reception.

153 The image acquisition parameters are given in Table 1 and the protocol is shown in Figure 1. Axial  $T_1$ -  
 154 RARE images were acquired using the scanner default parameters for the purpose of brain region  
 155 delineation (Figure 1, dataset A). Coronal multi-flip angle spoiled gradient echo (SPGR) sequences  
 156 were acquired at multiple TRs (long TR using 2D SPGR and short TR using 3D SPGR) to allow  
 157 combined estimation of flip angle error ( $k$ ) and pre-contrast  $T_1$  in blood and each brain region (Figure  
 158 1; dataset B). For short TR data, 10 gradient echoes were acquired per RF excitation to allow  
 159 correction for  $T_2^*$  decay. Dynamic SPGR acquisitions (Figure 1, datasets C and E) were collected for  
 160 estimation of trans-BBB contrast agent leakage rate,  $K^{trans}$ . These scans had a short TR to *minimize*  
 161 sensitivity to  $\tau_b$ , and high spatial resolution to enable sampling of blood signal from the superior  
 162 sagittal sinus (SSS), free from partial volume effects. Gadoteric acid (Dotarem, Guerbet; dose = 0.5  
 163  $\text{mmol kg}^{-1}$ ) was injected intravenously on the 6th volume of dataset C through a 24G cannular  
 164 inserted into the tail vein with a pump at  $1 \text{ mL min}^{-1}$ . After equilibration of the contrast agent  
 165 throughout the blood pool (at approximately 2.5 minutes following first pass), dataset D was collected  
 166 to estimate  $PS_w$ . Dataset D had a long TR, large voxels, and multiple repetitions, to *maximize*  
 167 sensitivity to  $\tau_b$ . Multiple flip angles were used to provide differential sensitivity to  $p_b$  and  $\tau_b$ , as shown  
 168 in Figure 3a-b. The slice/slab select direction was placed along the superior-inferior direction (coronal  
 169 slices) to ensure non-selective excitation of spins along the rostral-caudal direction to minimize  $T_1$   
 170 inflow effects.

### 171 1.2.5 Analysis pipeline

172 The data analysis pipeline is shown in Figure 2. Signals were corrected for  $T_2^*$  decay by fitting a  
 173 mono-exponential decay model to multi-gradient echo data (Figure 2a), providing estimates of the  
 174 signal magnitude at zero echo time,  $S(TE = 0)$ . Flip angle error ( $k = \alpha/\alpha_0$ , where  $\alpha$  is the delivered flip  
 175 angle, and  $\alpha_0$  the prescribed flip angle at the scanner console) and pre-contrast  $T_1$  were mapped  
 176 voxel-wise by jointly fitting SPGR signal models to multi-TR multi-flip angle data (Dickie et al., 2015;

177 Voigt et al., 2010) (Figure 2b). Linear interpolation was used to up-sample long TR data to the matrix  
 178 size of the short TR data. MRI signals from hippocampal, cortical, striatal, and thalamic regions were  
 179 extracted for each rat by registering the high resolution  $T_1$ -RARE image (Figure 1; dataset A) to the  
 180 Schwarz et al. rat brain atlas (Schwarz et al., 2006). Image registration was performed using in-house  
 181 software written in Matlab (The Mathworks, Inc., Natick, Massachusetts, USA). Regional estimates of  
 182  $k$ ,  $T_1$ , and  $S(TE = 0)$  were obtained by taking the median from voxels in the region. Regional  
 183 estimates of  $PS_w$  were then obtained by fitting SPGR signal models for an exchanging two-site  
 184 system (Buckley et al., 2008) to regional multi-flip angle decay-corrected signals from dataset D:

185

$$S(TE = 0, t) = S_0 \left[ a_s(t) \frac{\sin \alpha \left( 1 - e^{-\frac{-TR}{T_{1,S}(t)}} \right)}{\left( 1 - \cos \alpha e^{-\frac{-TR}{T_{1,S}(t)}} \right)} + (1 - a_s(t)) \frac{\sin \alpha \left( 1 - e^{-\frac{-TR}{T_{1,L}(t)}} \right)}{\left( 1 - \cos \alpha e^{-\frac{-TR}{T_{1,L}(t)}} \right)} \right] \quad (3)$$

186

187 where  $S(TE = 0, t)$  is the MRI signal at zero echo time ( $TE = 0$ ) as a function of acquisition time,  $t$ ,  
 188  $a_s(t)$  is the apparent blood water population fraction,  $T_{1,S}(t)$  is the apparent intravascular  $T_1$  value in  
 189 the presence of trans-BBB water exchange, and  $T_{1,L}(t)$  is the apparent extravascular  $T_1$  value in the  
 190 presence of trans-BBB water exchange,  $\alpha$  is the delivered flip angle ( $\alpha = \alpha_0$ ), and TR is the repetition  
 191 time. The two-site one-exchange (2S1X) model solutions relate  $a_s$ ,  $T_{1,S}$ , and  $T_{1,L}$  to the true blood  
 192 water population fraction  $p_b$ , the mean blood water residence time  $\tau_b$ , and true intravascular and  
 193 extravascular  $T_1$  values ( $T_{1,b}$  and  $T_{1,e}$ , respectively) (Landis et al., 1999):

194

$$a_s = \frac{1}{2} - \frac{1}{2} \left( \frac{\left[ \left( \frac{1}{T_{1,e}} - \frac{1}{T_{1,b}(t)} \right) (2p_b - 1) + \frac{p_b}{(1-p_b)\tau_b} + \frac{1}{\tau_b} \right]}{\left[ \left( \frac{1}{T_{1,e}} - \frac{1}{T_{1,b}(t)} + \frac{p_b}{(1-p_b)\tau_b} - \frac{1}{\tau_b} \right)^2 + \frac{4p_b}{(1-p_b)\tau_b^2} \right]^{\frac{1}{2}}} \right) \quad (4)$$

$$\frac{1}{T_{1,S}(t)} = \frac{1}{2} \left[ \left( \frac{1}{T_{1,e}} + \frac{1}{T_{1,b}(t)} + \frac{p_b}{(1-p_b)\tau_b} + \frac{1}{\tau_b} \right) + \left[ \left( \frac{1}{T_{1,e}} - \frac{1}{T_{1,b}(t)} + \frac{p_b}{(1-p_b)\tau_b} - \frac{1}{\tau_b} \right)^2 + \frac{4p_b}{(1-p_b)\tau_b^2} \right]^{\frac{1}{2}} \right] \quad (5)$$

195

$$\frac{1}{T_{1,L}(t)} = \frac{1}{2} \left[ \left( \frac{1}{T_{1,e}} + \frac{1}{T_{1,b}(t)} + \frac{p_b}{(1-p_b)\tau_b} + \frac{1}{\tau_b} \right) - \left[ \left( \frac{1}{T_{1,e}} - \frac{1}{T_{1,b}(t)} + \frac{p_b}{(1-p_b)\tau_b} - \frac{1}{\tau_b} \right)^2 + \frac{4p_b}{(1-p_b)\tau_b^2} \right]^{\frac{1}{2}} \right] \quad (6)$$

196

197 The  $T_1$  relaxation time of extravascular water,  $T_{1,e}$ , was fixed to its pre-contrast value, effectively  
 198 enforcing an assumption of zero contrast agent leakage across the BBB. Before injection of the  
 199 contrast agent, we assume the fast-exchange limit holds and thus parametrise  $T_{1,e}$  in terms of pre-



200 contrast blood and tissue  $T_1$  values ( $T_{1,b}(t=0)$  and  $T_{1,t}(t=0)$ ), which were estimated through pre-  
 201 contrast  $T_1$  mapping, and  $p_b$ , which was unknown at the time of fitting:

$$T_{1,e} = \frac{(1 - p_b)}{\left(\frac{1}{T_{1,t}(t=0)} - \frac{p_b}{T_{1,b}(t=0)}\right)} \quad (7)$$

202

203 The  $T_1$  relaxation time of blood,  $T_{1,b}(t)$ , was estimated via the following expression:

$$\frac{1}{T_{1,b}(t)} = \frac{1}{T_{1,b}(t=0)} + r_1 C_b(t) \quad (8)$$

204

205 where  $r_1$  is the  $T_1$  relaxivity of gadoteric acid, set to  $3.5 \text{ (mM s)}^{-1}$  (Rohrer et al., 2005).  $T_{1,b}(t=0)$  and  
 206  $C_b(t)$ , and thus  $T_{1,b}(t)$ , were measured from the superior sagittal sinus (SSS) using datasets B, C and  
 207 E. SSS voxels were chosen as follows. A slice containing the SSS was manually selected from the 4<sup>th</sup>  
 208 post-contrast volume (SSS appears bright). A histogram of decay-corrected signals from this slice  
 209 was generated and voxels with  $S(\text{TE} = 0)$  in the 99th percentile of all signals in the slice were  
 210 selected. Quality control checks were performed to ensure these voxels did indeed arise from the  
 211 SSS, and not from other vessels in the brain. Pre-contrast  $T_1$  of blood,  $T_{1,b}(t=0)$ , was estimated from  
 212 dataset B by taking the median  $T_{1b}$  value from selected SSS voxels.  $C_b(t)$  was estimated from the  
 213 median SSS signal acquired during C and E, using knowledge of  $T_{1,b}(t=0)$  estimated from dataset B.  
 214 During dataset D,  $C_b(t)$  was not measured directly, but inferred from a bi-exponential fit to  $C_b(t)$   
 215 measured in C and E (Figure 2d). Therefore, the only unknowns during fitting of Eqn. 3 to dataset D  
 216 were  $p_b$ ,  $T_b$ , and  $S_0$ .

217 Estimates of the permeability surface-area product to water,  $PS_w$ , were obtained from the ratio of  $p_b$   
 218 and  $\tau_b$ , scaled by the brain-blood partition coefficient for water,  $\lambda$ . We assumed  $\lambda$  is uniform across the  
 219 brain and equal to 0.9 (Herscovitch and Raichle, 1985). The trans-BBB leakage rate of contrast agent,  
 220  $K^{\text{trans}}$ , was estimated by fitting the Patlak model (Patlak et al., 1983) to datasets C and E. To  
 221 reproduce Patlak model analyses present in the literature (Montagne et al., 2015; van de Haar et al.,  
 222 2016) blood and tissue concentrations were derived from the first gradient echo ( $\text{TE} = 2.09 \text{ ms}$ ), not  
 223 the decay corrected signal. All model fitting was done in statistical software package R (Version 3.1, R  
 224 Foundation for Statistical Computing, Vienna, Austria).

225 The noise-to-signal ratio of extracted curves was estimated in five randomly selected rats and used to  
 226 infer parameter CoV using results from Monte Carlo simulations. Noise-to-signal ratio was estimated  
 227 by dividing the standard deviation of signal, computed from the first six flip angle images of dataset D,  
 228 by the equilibrium signal ( $S_0$ ) estimated from model fitting. Using the measured noise-to-signal ratios,  
 229 the parameter CoV was inferred using the data from Figure 3d as a look-up table.

### 230 1.2.6 Post-hoc protocol appraisal

231 To evaluate possible time-saving modifications to our imaging protocol, Eqn. 3 was re-fitted to dataset  
 232 D using only 2 or 3 of the 6 available repeats collected for each flip angle. Bland-Altman plots showing  
 233 the difference in parameter estimates were generated and the null hypothesis of no differences in the  
 234 mean and variance of parameter estimates tested using t- and F-tests, respectively.

### 235 1.2.7 Immunofluorescent staining, imaging, and quantification

236 Following MRI, the brains of all animals were collected and underwent immunohistochemistry to  
 237 visualize proteins linked to the tight junctions (occludin, claudin-5) and membrane water channels  
 238 (aquaporin-4). All proteins were dual stained with lectin to visualize vessels. Slides were imaged at  
 239 40x using a 3D Histech Panoramic P250 Flash slide scanner and the area of staining quantified

240 using in-house software. In transgenic rats, lectin led to aspecific staining of amyloid- $\beta$  plaques. No  
 241 amyloid- $\beta$  staining was observed in wild-types. To avoid bias in derived statistics between TgF344-AD  
 242 and wild-types, amyloid- $\beta$  plaques were delineated manually on lectin images in ImageJ (v1.51,  
 243 National Institute of Health, USA) and excluded from quantification of lectin and marker expression.  
 244 Full details of immunohistochemistry, slide imaging, and quantification are given in supplementary  
 245 materials.

### 246 1.2.8 Statistical analysis of MRI and immunofluorescent data

247 Two way analysis of variance (ANOVA) with effects of genotype and region (plus the genotype-region  
 248 interaction) were performed on estimates of  $PS_w$ ,  $K^{trans}$ , and all immunostains. Region was input as a  
 249 repeated measure. Based on the ANOVA results,  $PS_w$  and  $K^{trans}$  measures were correlated against  
 250 occludin (% snapshot area), i) in each brain region ignoring group status, ii) averaging  $PS_w$ ,  $K^{trans}$ , and  
 251 occludin across the four brain regions and computing independent correlations for TgF344-AD and  
 252 wildtype rats. Correlation coefficients were tested for statistical significance against the null  
 253 hypothesis of zero correlation. All statistical analyses were done in R (Version 3.1, R Foundation for  
 254 Statistical Computing, Vienna, Austria). No corrections were made for multiple comparisons.

## 255 1.3 Results

### 256 1.3.1. Sensitivity analysis

257 Our simulations show  $\tau_b$  and  $p_b$  sensitivity varies with both excitatory flip angle ( $\alpha$ ) and repetition time  
 258 (TR) (Figure 3a-b). In both cases, sensitivity profiles for  $p_b$  and  $\tau_b$  diverge, suggesting either approach  
 259 (varying flip angle, or varying TR) could be used to estimate these parameters from MRI data.  
 260 Sensitivity to  $\tau_b$  was maximum at intermediate flip angles and at longer TRs. Sensitivity to  $p_b$  was  
 261 maximum at large flip angles and short TRs. Sensitivity to  $\tau_b$  was near zero at low blood contrast  
 262 agent concentrations ( $C_b \sim 0$ ), and increased linearly with  $C_b$  up to approximately 4mM, after which  
 263 sensitivity increased more slowly (Figure 3c). Sensitivity to  $p_b$  plateaued at a lower  $C_b$  than  $\tau_b$ .

### 264 1.3.2. Monte Carlo Simulations

265 In MFAME-MRI, we opt to vary flip angle, while using a relatively long, fixed TR (100 ms), such that  
 266  $T_2^*$  decay can be quantified and corrected in all images using an invariant multi-gradient echo  
 267 readout. Figure 3d shows how the CoV in  $PS_w$  is reduced by using more unique flip angles rather than  
 268 acquiring more repeats of the same flip angles, up to approximately 5 angles, after which CoV does  
 269 not decrease further. In MFAME-MRI we use 5 flip angles centred around  $30^\circ$ . The highest flip angle  
 270 is increased from  $50^\circ$  to  $80^\circ$  to obtain a single image with very high sensitivity to  $p_b$  but low sensitivity  
 271 to  $\tau_b$  (see Figure 3a).

272 Simulations showed that flip angle error caused by  $B_1^+$  field inhomogeneity produces substantial  
 273 biases in all parameters (black lines in Figure 3e). Estimating flip angle error directly from multi-TR  
 274 multi-flip angle data, alongside pre-contrast  $T_1$ , successfully removed these biases (overlapping red  
 275 lines in Figure 3e). This correction method was implemented in the rat experiments. Non-zero  $K^{trans}$   
 276 caused overestimation of  $p_b$  and  $\tau_b$ , however, because  $PS_w$  is the ratio of these measures, it was  
 277 mostly unaffected ( $< 8\%$  bias up to  $K^{trans} = 10^{-3} \text{ min}^{-1}$ ; Figure 3f).

### 278 1.3.3 Animal experiments

279 ANOVA analyses revealed that  $PS_w$  differed between genotype ( $p = 0.0022$ ; higher  $PS_w$  in TgF344-AD  
 280 rats), but not between brain region ( $p = 0.93$ ) (Figure 4a). There was no genotype-region interaction  
 281 effect ( $p = 0.85$ ). While ANOVA analyses suggest the magnitude of  $PS_w$  alterations are not region  
 282 dependent (between the regions studied), the plotted data in Figure 4a show that the largest changes  
 283 occur in the hippocampus, striatum and thalamus, with the smallest effect in the cortex. The trans-  
 284 BBB leakage rate of MRI contrast agent ( $K^{trans}$ ) did not differ significantly between transgenic and



285 wild-type animals ( $p = 0.477$ ) or between brain region ( $p = 0.226$ ), and had no genotype-region  
286 interaction ( $p = 0.97$ ) (Figure 4b).

287 As  $PS_w$  was hypothesized to be closely related to BBB integrity, we assessed by  
288 immunohistochemistry vessel area by lectin and the expression of three different BBB markers: two  
289 tight junction proteins (occludin and claudin-5) and a water channel protein (aquaporin-4). ANOVA  
290 analyses revealed a genotype effect for occludin ( $p = 0.0061$ ), but no region effect ( $p = 0.64$ ) or  
291 genotype-region interaction ( $p = 0.92$ ). Claudin-5 and aquaporin-4 did not display any genotype ( $p =$   
292  $0.58$  and  $p = 0.73$  respectively), region ( $p = 0.070$  and  $p = 0.38$  respectively), or genotype-region  
293 interaction effects ( $p = 0.32$  and  $p = 0.43$  respectively – Figures 4e-f). Vessel area as quantified by  
294 lectin staining did not differ significantly between transgenic and wild-types ( $p = 0.27$ , Figure 4g), but  
295 did differ between brain region ( $p < 3 \times 10^{-5}$ ). Region specific correlation analyses showed that rats  
296 with lower occludin had higher  $PS_w$  (Figure 4h). In these plots, correlations were driven by both within-  
297 and between-group variability. Because vessel area assessed by lectin did not differ significantly  
298 between genotype, genotype differences in occludin and  $PS_w$  were most likely due to altered  
299 expression of the protein per unit vessel length (and therefore indicative of reduced BBB integrity),  
300 and not due to reduced vessel surface area or density. When estimates of  $PS_w$  and occludin were  
301 averaged across the four brain regions and each group treated independently, correlations remained  
302 statistically significant (Figure 4i) indicating that  $PS_w$  is sensitive to natural occludin variation present  
303 within both TgF344-AD and wild-type groups.  $K^{trans}$  did not correlate with occludin.

304 The noise-to-signal ratios of *in-vivo* regional multi-flip angle curves were between 0.001-0.003  
305 (corresponding to signal-to-noise ratios of 333-1000). Using the data presented in Figure 3d as a  
306 look-up table, these noise-to-signal ratios gave predicted *in-vivo* parameter CoV values of 10-20% for  
307  $p_b$ , 10-30% for  $\tau_b$ , and 15-45% for  $PS_w$ , dependent on brain region. Noise-to-signal ratios, and thus  
308 predicted CoV values, were largest for the hippocampus, and smallest for the cortex.

309 Figure 5 shows the results of the post hoc protocol appraisal. Estimating  $PS_w$  using only two of the six  
310 available image repeats collected for dataset D did not significantly alter the central tendency (mean)  
311 ( $p = 0.22$ ) or variance (precision) ( $p = 0.80$ ) of  $PS_w$  estimates. Using 3 repeats also led to similar  
312 results ( $p = 0.21$  and  $p = 0.22$ ).

#### 313 1.4 Discussion

314 BBB breakdown is known to occur with ageing and could be exacerbated in AD, accelerating disease  
315 pathogenesis and associated cognitive decline (Sweeney et al., 2018; Zlokovic, 2011). While a  
316 number of studies have shown an interaction between  $A\beta$  and tight junction proteins (Keaney et al.,  
317 2015; Kook et al., 2012), the impact of AD pathology on BBB breakdown has been difficult to robustly  
318 demonstrate *in-vivo*. A recent study evaluating BBB disruption in a variety of AD mouse models failed  
319 to detect AD-related differences in the blood-brain leakage of injected probes (Bien-Ly et al., 2015). A  
320 meta-analysis of cerebrospinal fluid assay and imaging studies also failed to infer a statistically  
321 significant effect of AD on BBB integrity (Farrall and Wardlaw, 2009). However, recent prospective  
322 human studies using advanced dynamic contrast-enhanced MRI have been able to detect increased  
323 leakage of contrast agent across the BBB in patients with mild-cognitive impairment (Montagne et al.,  
324 2015) and in early AD (van de Haar et al., 2016), supporting an argument for AD-related BBB  
325 damage. In our study of the TgF344-AD rat model, we fail to detect any increase in BBB permeability  
326 to MRI contrast agent, but do detect increased permeability to water, indicating MFAME-MRI may be  
327 more sensitive than available 'tracer leakage' methods and could provide a more useful marker of  
328 subtle BBB breakdown.

329 The consequence of subtle BBB damage is unknown. It is unlikely to impact the trans-BBB transport  
330 of large molecules. More likely is that such changes (i.e., increased water-exchange) will impact ion  
331 homeostasis and brain water balance (Amiry-Moghaddam and Ottersen, 2003) which is required for  
332 proper functioning of neuronal circuits. Furthermore, if BBB damage is a crucial early event in AD

333 pathogenesis, methods such as those presented here will be extremely useful for studying the timing  
334 and order of BBB changes when they first occur, and possibly for monitoring the response of novel  
335 BBB-targeted therapeutics.

336 The overall measurement time used in this study was long, presenting a potential barrier for  
337 implementation of this exact protocol to scan human patients with dementia. Figure 1 shows scan  
338 time is approximately split between pre-contrast  $B_1^+$ - $T_1$  mapping and post-contrast measurements. In  
339 a clinical setting, less time-consuming flip angle mapping approaches based on Bloch-Siegert shift  
340 could be used (Sacolick et al., 2010). Examination of Figure 3b shows reductions in TR could be  
341 implemented, reducing down to 75 or 50 ms, with little effect on the precision of  $\tau_b$ . Such changes may  
342 actually increase precision in  $PS_w$  through increased sensitivity to  $p_b$ , however simulations are  
343 required to test this hypothesis. Furthermore, additional time saving modifications to our method may  
344 be gained by acquiring fewer repetitions per unique flip angle, which we show does not significantly  
345 alter the central tendency or precision of  $PS_w$  estimates. Last, since MFAME-MRI uses multiple flip  
346 angles to gain  $PS_w$  sensitivity and multiple TRs for estimation of flip angle error, reductions in scan  
347 time may also be gained by using an MR fingerprinting approach (Ma et al., 2013).

348 Our approach uses standard MRI contrast agents, which leak across the BBB unless the BBB is fully  
349 intact. The modelling used here to estimate  $PS_w$  assumes that no leakage occurs, which may not be  
350 true due to age- (Montagne et al., 2015) or cerebrovascular disease (Farrall and Wardlaw, 2009)  
351 related BBB breakdown. However, we show that at the leakage levels expected in dementia patients  
352 ( $10^{-5} - 10^{-3} \text{ min}^{-1}$ ), and for those levels measured in TgF344-AD rats in this study ( $\sim 1-3 \times 10^{-4} \text{ min}^{-1}$ ),  
353 leakage of contrast agent does not substantially impact estimates of  $PS_w$  (Figure 3f). Furthermore, it  
354 may still be possible to use our MFAME-MRI approach in stroke or tumours where leakage of contrast  
355 agent is greater, however a generalised water-exchange model that accounts for non-zero  $K^{\text{trans}}$   
356 would be required (Li et al., 2005). Other MRI approaches have been proposed for quantifying trans-  
357 BBB water-exchange which do not rely on injection of exogenous tracers; e.g. diffusion-weighted  
358 arterial spin labelling MRI (Silva et al., 1997; St. Lawrence et al., 2012). However, these techniques  
359 are usually limited to estimation of  $\tau_b$ , which is likely to be a less physiologically specific measure of  
360 BBB integrity due to its co-dependence on both  $PS_w$  and  $p_b$ .

361 The study had the following limitations. Aspecific staining of amyloid plaques was observed in lectin  
362 immuno-stains of transgenic rats, but not in wildtypes. Since such plaques were large in size relative  
363 to vessels (see Figure 4c and Supplementary Figure 1), the snapshot image area covered by such  
364 plaques was removed from analyses, and snapshot statistics adjusted accordingly. If amyloid plaques  
365 were present in regions of highest or lowest vessel density, it is possible that such a procedure could  
366 have biased quantification of lectin, occludin, claudin-5, and aquaporin-4, artificially reducing or  
367 increasing the '% of snapshot' quantified respectively, relative to wild-types. However, we did not see  
368 a favoured pattern of amyloid deposition visually, and believe that such biasing is unlikely. Aspecific  
369 staining of vascular amyloid may have also occurred in lectin immuno-stains, however due to the  
370 proximity of vascular amyloid deposits to the vessel lumen, it was not possible to ascertain if this was  
371 present, and if so correct for it. Such staining, if non-negligible, would have led to an artefactual  
372 increase in the amount of lectin classified as vessel in TgF344-AD rats, relative to wild-types. The  
373 animals used were relatively old ( $\sim 18$  months). Their age at time of scanning was chosen primarily to  
374 maximise the severity of AD pathology and thus AD-related BBB damage. It is possible that age-  
375 related BBB damage may also have been present, which would also have presented in wild-types,  
376 and could be a possible explanation for some of the within-group variation that is observed,  
377 particularly in the wild type animals. The relative magnitude of age and AD-related BBB damage is  
378 currently unknown and should be investigated in future studies, both in animal models and humans.  
379 The rats were not culled immediately following scanning. Some BBB damage may have occurred  
380 between scanning and culling, which may have added variability to MRI and immunohistochemistry  
381 comparisons, worsening correlations. However, since the time delay was only a small fraction of the  
382 entire lifetime of the animal, we expect this effect to be minimal.

383 In summary, we have demonstrated MFAME-MRI can non-invasively detect subtle BBB permeability  
 384 alterations in a rat model of AD, related to decreased expression of the BBB tight junction protein  
 385 occludin. Until now, MRI techniques have focused on measuring the leakage of hydrophilic passively  
 386 dispersed exogenous probes. However, when BBB breakdown is subtle, as may be the case in AD,  
 387 such probes leak very slowly, resulting in low measurement sensitivity. MFAME-MRI is a new  
 388 promising tool to study subtle BBB damage, potentially enabling detection of cerebrovascular  
 389 pathology far earlier in disease pathogenesis than previously possible.

### 390 1.5 Data availability statement

391 The data that support the findings of this study are available from the corresponding author upon  
 392 reasonable request.

### 393 1.6 Acknowledgments

394  
 395 The authors would like to thanks Mrs Lidan Christie and Karen Davies for their technical contribution.  
 396

### 397 1.7 Funding

398  
 399 The purchase of the TgF344-AD rat was jointly supported by the European Union's Seventh  
 400 Framework Programme (FP7/2007-2013) under grant agreement n° HEALTH-F2-2011-278850  
 401 (INMiND) and Alzheimer Research UK network funds. The breeding and maintenance of the TgF344-  
 402 AD rat was supported by the European Union's Seventh Framework Programme (FP7/2007-2013)  
 403 under grant agreement n° HEALTH-F2-2011-278850 (INMiND). BD, MV as well as scanning of the  
 404 TgF344-AD rats were funded by the EPSRC project EP/M005909/1. The MRI facility is supported  
 405 through an equipment grant from BBSRC UK (BB/F011350).

### 406 1.8 Author Contributions

407 BD designed the MRI protocol, acquired the imaging data, and performed data analysis and statistics.  
 408 JU contributed to MRI protocol development and optimisation. MV performed immunostaining. GP, LP  
 409 and HB supervised the work and contributed to preparation of the manuscript.

### 410 1.9 Competing Interest Statement

411 GJMP is a shareholder and director of Bioxydyn Limited, a company with an interest in quantitative  
 412 imaging biomarkers  
 413  
 414

### 415 1.10 Figure Legends

416 **Figure 1.** The MRI protocol. Dataset A: high resolution  $T_1$ -RARE images for segmentation of key  
 417 brain regions in conjunction with the Schwarz et al. rat atlas. Dataset B: multi-repetition time (TR)  
 418 multi-flip angle spoiled gradient recalled echo (SPGR) images for combined flip angle error (k) and  
 419 pre-contrast  $T_1$  mapping. Datasets C and E: high spatial resolution dynamic SPGR images for  
 420 estimation of  $K^{\text{trans}}$  and monitoring contrast agent concentration in the superior sagittal sinus (SSS).  
 421 Dataset D: low spatial resolution multi-flip angle multi-echo (MFAME)-MRI SPGR images for  
 422 estimation of  $PS_w$ . Abbreviations: CA, contrast agent; k, flip angle error; TR, repetition time; TE, echo  
 423 time;  $n_{\text{rep}}$ , number of image repetitions.

424 **Figure 2.** Analysis pipeline for estimation of  $PS_w$  and  $K^{\text{trans}}$ . **a** A mono-exponential model is fit to multi-  
 425 gradient echo signals to correct for  $T_2^*$  decay, producing estimates of MRI signal at zero echo time,  
 426  $S(\text{TE} = 0)$ . **b** Maps of flip angle error (k) and pre-contrast  $T_1$  are estimated from short TR (red points)  
 427 and long TR (black points) data by jointly fitting the spoiled gradient echo (SPGR) signal model,  
 428 assuming the fast exchange limit for water exchange. Red and black lines show the joint fit to this  
 429 data. **c** Median MRI signals, k and  $T_1$  for each region are extracted by registering the  $T_1$ -weighted

430 RARE anatomic image to the Schwarz et al. atlas. Blood signals and associated  $k$  and  $T_1$  values are  
 431 extracted from the superior sagittal sinus (SSS) using a semi-automated procedure. **d** A bi-  
 432 exponential model is fit to measurements of blood contrast agent concentration ( $C_b$ ) from datasets C  
 433 and E. The model fit is used to infer  $C_b$  during dataset D. **e** The two-site one-exchange (2S1X) model  
 434 is fit to regional tissue curves from dataset D to estimate the mean blood water residence time ( $\tau_b$ ),  
 435 blood water population fraction ( $p_b$ ), and the trans-BBB permeability surface area product to water  
 436 ( $PS_w$ ). **f** The Patlak model is fit to regional tissue curves from datasets C and E to estimate the trans-  
 437 BBB leakage rate of contrast agent,  $K^{trans}$ . In a, b, d, e, and f, data points and fitted curves are  
 438 representative of the signal to noise ratio and fit quality of acquired rat data.

439 **Figure 3.** Sensitivity analysis and Monte Carlo simulations. **a-c** Sensitivity plots showing the  
 440 percentage increase or decrease in post-contrast MRI signal intensity due to a 50% increase in  $\tau_b$   
 441 (solid line) or  $p_b$  (dashed line) as a function of flip angle, TR, and blood contrast agent concentration  
 442 ( $C_b$ ). The dotted line denotes zero change in signal. **d** Coefficient of variation (CoV) of  $p_b$ ,  $\tau_b$ , and  $PS_w$   
 443 estimates (dotted line) as a function of noise-signal ratio for different unique flip angle and image  
 444 repeat combinations estimated from Monte Carlo simulations. Noise sd is the standard deviation of  
 445 zero mean Gaussian noise,  $S_0$  is the equilibrium signal. Symbols indicate the noise-to-signal ratio of  
 446 *in-vivo* rat data acquired with  $n_\alpha = 5$  (\* = hippocampus; + = cortex, \$ = striatum, # = thalamus). **e** The  
 447 effect of flip angle error ( $k = \alpha/\alpha_0$ ) on  $p_b$ ,  $\tau_b$ , and  $PS_w$  when assuming the delivered flip angle ( $\alpha$ ) is  
 448 equal to the prescribed flip angle ( $\alpha_0$ ) (black lines). The overlapping red lines show bias in parameter  
 449 estimates following flip angle error correction using multi-TR multi-flip angle data. **f** The effect of non-  
 450 zero  $K^{trans}$  on  $p_b$ ,  $\tau_b$ , and  $PS_w$ .

451 **Figure 4.** MRI and immunostaining results in TgF344-AD and wild-type rats. **a**  $PS_w$  is significantly  
 452 higher (up to 2-fold) in TgF344-AD rats relative to wild-types ( $p < 0.05$ ; two-way ANOVA). **b** Trans-  
 453 BBB leakage of contrast agent ( $K^{trans}$ ) is unaltered between TgF344-AD rats and wild-types ( $p =$   
 454  $0.477$ ; two-way ANOVA). **c** Representative occludin and lectin immuno-stains. Aspecific staining of  
 455 amyloid- $\beta$  was visually identified on the lectin snapshots and manually segmented as shown.  
 456 Segmented regions were then removed from the calculation of snapshot statistics. **d** Occludin is  
 457 reduced in TgF344-AD relative to wild-types ( $p < 0.05$ ; two-way ANOVA), corresponding well with  
 458 genotype differences in  $PS_w$ . **e** No detectable TgF344AD/wild-type differences were observed for  
 459 claudin-5 or, **f** aquaporin-4 (AQP4). **g** Lectin stains showed no difference in total vessel area between  
 460 TgF344-AD and wild-types ( $p = 0.27$ ; two-way ANOVA). **h**  $PS_w$  measurements correlated inversely  
 461 with occludin staining in all regions tested. **i** When estimates for each rat were averaged across the  
 462 four regions, and group-wise correlations computed, correlations maintained significance, confirming  
 463 that occludin can explain variability in  $PS_w$  independent of group. In h-i, black markers represent  
 464 TgF344-AD rats and white markers represent wild-types. In all plots, '% of snapshot' is the  
 465 percentage area of snapshot occupied by the immunostain, averaged across all snapshots taken for  
 466 that region. Data shown in a, b, d, e, f, and g are mean  $\pm$  s.e.m.

467 **Figure 5.** Post-hoc protocol appraisal. Bland-Altman plots show the difference in  $PS_w$  estimates  
 468 ( $\Delta PS_w$ ) when fitting to dataset D with 6 versus 2 repetitions per flip angle. In all regions, the use of 2  
 469 repetitions underestimated  $PS_w$  relative to 6 repetitions, but differences were not statistically  
 470 significant ( $p = 0.22$ ). Variance in  $PS_w$  across both groups was also unaltered ( $p = 0.80$ ). Black dots  
 471 represent TgF344-AD rats, while white dots represent wild-types. The solid dotted lines denotes  $\Delta PS_w$   
 472  $= 0$ , while the dotted horizontal lines denote the mean bias in  $\Delta PS_w$  between estimates using 6 vs 2  
 473 repeats.

474 **Supplementary Figure 1.** Representative claudin-5 and aquaporin-4 immuno-stains, and an example  
 475 of lectin segmentation. **a** Representative claudin-5 and lectin immuno-stains. **b** Representative  
 476 aquaporin-4 and lectin immuno-stains. Aspecific staining of amyloid- $\beta$  was visually identified on the  
 477 lectin snapshots and manually segmented. Segmented regions were then removed from calculation of  
 478 snapshot statistics. **c** An image of an entire sagittal section stained with lectin. Each animal had 4



479 such sections cut at different locations from bregma. The white box shows the relative size of 10x  
 480 snapshot images taken in the cortex, compared to the overall size of the section. **d** The corresponding  
 481 10x lectin image shown in **c** **e** The segmentation image derived by passing the lectin image in **d**  
 482 through the in-house segmentation pipeline.

### 483 1.11 Bibliography

- 484
- 485 Amiry-Moghaddam, M., Ottersen, O.P., 2003. The molecular basis of water transport in the brain. *Nat.*  
 486 *Rev. Neurosci.* 4, 991–1001. <https://doi.org/10.1038/nrn1252>
- 487 Armitage, P.A., Farrall, A.J., Carpenter, T.K., Doubal, F.N., Wardlaw, J.M., 2011. Use of dynamic  
 488 contrast-enhanced MRI to measure subtle blood–brain barrier abnormalities. *Magn. Reson.*  
 489 *Imaging* 29, 305–314. <https://doi.org/10.1016/j.mri.2010.09.002>
- 490 Bains, L.J., McGrath, D.M., Naish, J.H., Cheung, S., Watson, Y., Taylor, M. Ben, Logue, J.P., M.  
 491 Parker, G.J., Waterton, J.C., Buckley, D.L., 2010. Tracer kinetic analysis of dynamic contrast-  
 492 enhanced MRI and CT bladder cancer data: A preliminary comparison to assess the magnitude  
 493 of water exchange effects. *Magn. Reson. Med.* 60, n/a-n/a. <https://doi.org/10.1002/mrm.22430>
- 494 Bien-Ly, N., Boswell, C.A., Jeet, S., Beach, T.G., Hoyte, K., Luk, W., Shihadeh, V., Ulufatu, S.,  
 495 Foreman, O., Lu, Y., DeVoss, J., van der Brug, M., Watts, R.J., 2015. Lack of Widespread BBB  
 496 Disruption in Alzheimer’s Disease Models: Focus on Therapeutic Antibodies. *Neuron* 88, 289–  
 497 297. <https://doi.org/10.1016/j.neuron.2015.09.036>
- 498 Brix, G., Kiessling, F., Lucht, R., Darai, S., Wasser, K., Delorme, S., Griebel, J., 2004. Microcirculation  
 499 and microvasculature in breast tumors: pharmacokinetic analysis of dynamic MR image series.  
 500 *Magn. Reson. Med.* 52, 420–429.
- 501 Buckley, D.L., Kershaw, L.E., Staniszc, G.J., 2008. Cellular-interstitial water exchange and its effect on  
 502 the determination of contrast agent concentration in vivo: Dynamic contrast-enhanced MRI of  
 503 human internal obturator muscle. *Magn. Reson. Med.* 60, 1011–1019.  
 504 <https://doi.org/10.1002/mrm.21748>
- 505 Carrano, A., Hoozemans, J.J.M., van der Vies, S.M., Rozemuller, A.J.M., van Horsen, J., de Vries,  
 506 H.E., 2011. Amyloid Beta Induces Oxidative Stress-Mediated Blood–Brain Barrier Changes in  
 507 Capillary Amyloid Angiopathy. *Antioxid. Redox Signal.* 15, 1167–1178.  
 508 <https://doi.org/10.1089/ars.2011.3895>
- 509 Caserta, M.T., Caccioppo, D., Lapin, G.D., Ragin, a, Groothuis, D.R., Caserta, Mt, Caccioppo, D,  
 510 Lapin, Gd, 1998. Blood–brain barrier integrity in Alzheimer’s disease patients and elderly control  
 511 subjects. *J. ...* 10, 78–84.
- 512 Cohen, R.M., Rezai-Zadeh, K., Weitz, T.M., Rentsendorj, A., Gate, D., Spivak, I., Bholat, Y.,  
 513 Vasilevko, V., Glabe, C.G., Breunig, J.J., Rakic, P., Davtayan, H., Agadjanyan, M.G., Kepe, V.,  
 514 Barrio, J.R., Bannykh, S., Szekely, C.A., Pechnick, R.N., Town, T., 2013. A Transgenic  
 515 Alzheimer Rat with Plaques, Tau Pathology, Behavioral Impairment, Oligomeric A $\beta$ , and Frank  
 516 Neuronal Loss. *J. Neurosci.* 33, 6245–6256. <https://doi.org/10.1523/JNEUROSCI.3672-12.2013>
- 517 Dickie, B.R., Banerji, A., Kershaw, L.E., Mcpartlin, A., Choudhury, A., West, C.M., Rose, C.J., 2015.  
 518 Improved accuracy and precision of tracer kinetic parameters by joint fitting to variable flip angle  
 519 and dynamic contrast enhanced MRI data. *Magn. Reson. Med.* 76, 1270–1281.  
 520 <https://doi.org/10.1002/mrm.26013>
- 521 Donahue, K.M., Weisskoff, R.M., Burstein, D., 1997. Water diffusion and exchange as they influence  
 522 contrast enhancement. *J. Magn. Reson. Imaging* 7, 102–110.  
 523 <https://doi.org/10.1002/jmri.1880070114>
- 524 Dorr, A., Sahota, B., Chinta, L. V., Brown, M.E., Lai, A.Y., Ma, K., Hawkes, C.A., McLaurin, J.,  
 525 Stefanovic, B., 2012. Amyloid- $\beta$ -dependent compromise of microvascular structure and function  
 526 in a model of Alzheimer’s disease. *Brain* 135, 3039–3050. <https://doi.org/10.1093/brain/aws243>
- 527 Farrall, A.J., Wardlaw, J.M., 2009. Blood–brain barrier: Ageing and microvascular disease –  
 528 systematic review and meta-analysis. *Neurobiol. Aging* 30, 337–352.  
 529 <https://doi.org/10.1016/j.neurobiolaging.2007.07.015>
- 530 Herscovitch, P., Raichle, M.E., 1985. What is the correct value for the brain–blood partition coefficient  
 531 for water? *J. Cereb. Blood Flow Metab.* 5, 65–69. <https://doi.org/10.1038/jcbfm.1985.9>
- 532 Heye, A.K., Thrippleton, M.J., Armitage, P.A., Valdés Hernández, M. del C., Makin, S.D., Glatz, A.,  
 533 Sakka, E., Wardlaw, J.M., 2016. Tracer kinetic modelling for DCE-MRI quantification of subtle  
 534 blood-brain barrier permeability. *Neuroimage* 125, 446–455.  
 535 <https://doi.org/10.1016/j.neuroimage.2015.10.018>
- 536 Joo, I.L., Lai, A.Y., Bazzigaluppi, P., Koletar, M.M., Dorr, A., Brown, M.E., Thomason, L.A.M., Sled,  
 537 J.G., McLaurin, J., 2017. Early neurovascular dysfunction in a transgenic rat model of Alzheimer ’

- s disease. *Nat. Publ. Gr.* 1–14. <https://doi.org/10.1038/srep46427>
- 539 Keaney, J., Walsh, D.M., Malley, T.O., Hudson, N., Darragh, E., Loftus, T., Sheehan, F., Mcdaid, J.,  
 540 Humphries, M.M., Callanan, J.J., Brett, F.M., Farrell, M.A., Humphries, P., Campbell, M., 2015.  
 541 Autoregulated paracellular clearance of amyloid- $\beta$  across the blood-brain barrier. *Sci Adv.* 1, 1–  
 542 24. <https://doi.org/10.1126/sciadv.1500472>. Autoregulated
- 543 Kilkenny, C., Browne, W., Cuthill, I., Emerson, M., Altman, D., 2010. Animal research: Reporting in  
 544 vivo experiments: The ARRIVE guidelines. *Br. J. Pharmacol.* 160, 1577–1579.  
 545 <https://doi.org/10.1113/expphysiol.2010.053793>
- 546 Kook, S.-Y., Hong, H.S., Moon, M., Ha, C.M., Chang, S., Mook-Jung, I., 2012. A 1-42-RAGE  
 547 Interaction Disrupts Tight Junctions of the Blood-Brain Barrier Via Ca<sup>2+</sup>-Calcineurin Signaling. *J.*  
 548 *Neurosci.* 32, 8845–8854. <https://doi.org/10.1523/JNEUROSCI.6102-11.2012>
- 549 Landis, C.S., Li, X., Telang, F.W., Molina, P.E., Palyka, I., Vetek, G., Springer, C.S., 1999. Equilibrium  
 550 transcytolemmal water-exchange kinetics in skeletal muscle in vivo. *Magn. Reson. Med.* 42,  
 551 467–478. [https://doi.org/10.1002/\(SICI\)1522-2594\(199909\)42:3<467::AID-MRM9>3.0.CO;2-0](https://doi.org/10.1002/(SICI)1522-2594(199909)42:3<467::AID-MRM9>3.0.CO;2-0)
- 552 Li, X., Rooney, W.D., Springer, C.S., 2005. A unified magnetic resonance imaging pharmacokinetic  
 553 theory: Intravascular and extracellular contrast reagents. *Magn. Reson. Med.* 54, 1351–1359.  
 554 <https://doi.org/10.1002/mrm.20684>
- 555 Ma, D., Gulani, V., Seiberlich, N., Liu, K., Sunshine, J.L., Duerk, J.L., Griswold, M.A., 2013. Magnetic  
 556 resonance fingerprinting. *Nature* 495, 187–192. <https://doi.org/10.1038/nature11971>
- 557 Montagne, A., Barnes, S.R., Sweeney, M.D., Halliday, M.R., Sagare, A.P., Zhao, Z., Toga, A.W.,  
 558 Jacobs, R.E., Liu, C.Y., Amezcua, L., Harrington, M.G., Chui, H.C., Law, M., Zlokovic, B. V.,  
 559 2015. Blood-Brain barrier breakdown in the aging human hippocampus. *Neuron* 85, 296–302.  
 560 <https://doi.org/10.1016/j.neuron.2014.12.032>
- 561 Montagne, A., Nation, D.A., Sweeney, M.D., Toga, A.W., 2016. Brain imaging of neurovascular  
 562 dysfunction in Alzheimer's disease. *Acta Neuropathol.* [https://doi.org/10.1007/s00401-016-1570-](https://doi.org/10.1007/s00401-016-1570-0)  
 563 0
- 564 Patlak, C.S., Blasberg, R.G., Fenstermacher, J.D., 1983. Graphical evaluation of blood-to-brain  
 565 transfer constants from multiple-time uptake data. *J. Cereb. Blood Flow Metab.* 3, 1–7.  
 566 <https://doi.org/10.1038/jcbfm.1985.87>
- 567 Rohrer, M., Bauer, H., Mintorovitch, J., Requardt, M., Weinmann, H.-J., 2005. Comparison of  
 568 magnetic properties of MRI contrast media solutions at different magnetic field strengths. *Invest.*  
 569 *Radiol.* 40, 715–724. <https://doi.org/10.1097/01.rli.0000184756.66360.d3>
- 570 Sacolick, L.I., Wiesinger, F., Hancu, I., Vogel, M.W., 2010. B 1 mapping by Bloch-Siegert shift. *Magn.*  
 571 *Reson. Med.* 63, 1315–1322. <https://doi.org/10.1002/mrm.22357>
- 572 Schlageter, N.L., Carson, R.E., Rapoport, S.I., 1987. Examination of blood-brain barrier permeability  
 573 in dementia of the Alzheimer type with [68Ga]EDTA and positron emission tomography. *J.*  
 574 *Cereb. Blood Flow Metab.* 7, 1–8. <https://doi.org/10.1038/jcbfm.1987.1>
- 575 Schwarz, A.J., Danckaert, A., Reese, T., Gozzi, A., Paxinos, G., Watson, C., Merlo-Pich, E. V.,  
 576 Bifone, A., 2006. A stereotaxic MRI template set for the rat brain with tissue class distribution  
 577 maps and co-registered anatomical atlas: Application to pharmacological MRI. *Neuroimage* 32,  
 578 538–550. <https://doi.org/10.1016/j.neuroimage.2006.04.214>
- 579 Schwarzbauer, C., Morrissey, S.P., Deichmann, R., Hillenbrand, C., Syha, J., Adolf, H., Nöth, U.,  
 580 Haase, A., 1997. Quantitative magnetic resonance imaging of capillary water permeability and  
 581 regional blood volume with an intravascular {MR} contrast agent. *Magn Reson Med* 37, 769–  
 582 777.
- 583 Silva, A.C., Williams, D.S., Koretsky, A.P., 1997. Evidence for the exchange of arterial spin-labeled  
 584 water with tissue water in rat brain from diffusion-sensitized measurements of perfusion. *Magn.*  
 585 *Reson. Med.* 38, 232–7. <https://doi.org/10.1002/mrm.1910380211>
- 586 St. Lawrence, K.S., Owen, D., Wang, D.J.J., 2012. A two-stage approach for measuring vascular  
 587 water exchange and arterial transit time by diffusion-weighted perfusion MRI. *Magn. Reson.*  
 588 *Med.* 67, 1275–1284. <https://doi.org/10.1002/mrm.23104>
- 589 Starr, J.M., Farrall, A.J., Armitage, P., McGurn, B., Wardlaw, J., 2009. Blood-brain barrier permeability  
 590 in Alzheimer's disease: a case-control MRI study. *Psychiatry Res.* 171, 232–241.  
 591 <https://doi.org/10.1016/j.psychresns.2008.04.003>
- 592 Sweeney, M.D., Sagare, A.P., Zlokovic, B. V., 2018. Blood-brain barrier breakdown in Alzheimer  
 593 disease and other neurodegenerative disorders. *Nat. Rev. Neurol.* 14, 133–150.  
 594 <https://doi.org/10.1038/nrneurol.2017.188>
- 595 van de Haar, H.J., Burgmans, S., Hofman, P.A.M., Verhey, F.R.J., Jansen, J.F.A., Backes, W.H.,  
 596 2014. Blood-brain barrier impairment in dementia: Current and future in vivo assessments.  
 597 *Neurosci. Biobehav. Rev.* 49C, 71–81. <https://doi.org/10.1016/j.neubiorev.2014.11.022>



- 598 van de Haar, H.J., Burgmans, S., Jansen, J.F.A., van Osch, M.J.P., van Buchem, M.A., Muller, M.,  
599 Hofman, P.A.M., Verhey, F.R.J., Backes, W.H., 2016. Blood-Brain Barrier Leakage in Patients  
600 with Early Alzheimer Disease. *Radiology* 281, 527–535.  
601 <https://doi.org/10.1148/radiol.2016152244>
- 602 Vinters, H. V., 1987. Cerebral amyloid angiopathy. A critical review. *Stroke*. 18, 311–24.  
603 <https://doi.org/10.1161/01.STR.18.2.311>
- 604 Voigt, T., Nehrke, K., Doessel, O., Katscher, U., 2010. T1 corrected B1 mapping using multi-TR  
605 gradient echo sequences. *Magn. Reson. Med.* 64, 725–733. <https://doi.org/10.1002/mrm.22333>
- 606 Wang, Z., Su, M.Y., Nalcioglu, O., 1998. Measurement of tumor vascular volume and mean  
607 microvascular random flow velocity magnitude by dynamic Gd-DTPA-albumin enhanced and  
608 diffusion-weighted MRI. *Magn. Reson. Med.* 40, 397–404.  
609 <https://doi.org/10.1002/mrm.1910400309>
- 610 Weller, R.O., Subash, M., Preston, S.D., Mazanti, I., Carare, R.O., 2008. Perivascular drainage of  
611 amyloid- $\beta$  peptides from the brain and its failure in cerebral amyloid angiopathy and Alzheimer's  
612 disease. *Brain Pathol.* 18, 253–266. <https://doi.org/10.1111/j.1750-3639.2008.00133.x>
- 613 Yarnykh, V.L., 2007. Actual flip-angle imaging in the pulsed steady state: A method for rapid three-  
614 dimensional mapping of the transmitted radiofrequency field. *Magn. Reson. Med.* 57, 192–200.  
615 <https://doi.org/10.1002/mrm.21120>
- 616 Zhang, X., Petersen, E.T., Ghariq, E., De Vis, J.B., Webb, A.G., Teeuwisse, W.M., Hendrikse, J., Van  
617 Osch, M.J.P., 2013. In vivo blood T1 measurements at 1.5 T, 3 T, and 7 T. *Magn. Reson. Med.*  
618 70, 1082–1086. <https://doi.org/10.1002/mrm.24550>
- 619 Zlokovic, B. V., 2011. Neurovascular pathways to neurodegeneration in Alzheimer's disease and  
620 other disorders. *Nat. Rev. Neurosci.* 12, 723–739. <https://doi.org/10.1038/nrn3114>  
621

Table 1. MFAME-MRI acquisition parameters.

|                                  | Dataset                                      |   |   |   |                               |                                  |
|----------------------------------|--|---|---|---|-------------------------------|----------------------------------|
|                                  | A  | B (long TR)                                     | B (short TR)                                    | C   | D                             | E                                |
| <b>Pulse sequence</b>            | T <sub>1</sub> w RARE                        | SPGR  | Multi-echo SPGR                                 | Multi-echo SPGR   | Multi-echo SPGR               | Multi-echo SPGR                  |
| <b>Orientation</b>               | Axial  | Coronal   | Coronal   | Coronal   | Coronal                       | Coronal                          |
| <b>Acquisition type</b>          | 2D   | 2D  | 3D  | 3D  | 3D                            | 3D                               |
| <b>Flip angle (°)</b>            | 90   | 5, 10, 20, 30, 40, 60, 80, 90                   | 5, 10, 40, 60                                   | 60  | 30, 40, 20, 10, 80            | 60                               |
| <b>TR (ms)</b>                   | 1500   | 5000  | 100   | 20  | 100                           | 20                               |
| <b>TE (ms)</b>                   | 7  | 2.1   | 2.1   | 2.1   | 2.1                           | 2.1                              |
| <b>ΔTE (ms)</b>                  | N/A  | N/A   | 2.1   | 2.1   | 2.1                           | 2.1                              |
| <b># gradient echoes</b>         | N/A  | 1   | 10  | 6   | 10                            | 6                                |
| <b>FOV (mm)</b>                  | 30 x 30 x 30                                 | 30 x 30 x 30                                    | 30 x 30 x 30                                    | 30 x 30 x 30  | 30 x 30 x 30                  | 30 x 30 x 30                     |
| <b>Acquired Matrix size</b>      | 256 x 256                                    | 32 x 16   | 64 x 32 x 48                                    | 64 x 32 x 48  | 32 x 16 x 16                  | 64 x 32 x 48                     |
| <b>Reconstructed Matrix size</b> | 256 x 256                                    | 32 x 32   | 64 x 64 x 96                                    | 64 x 64 x 96  | 32 x 32 x 32                  | 64 x 64 x 96                     |
| <b># slices</b>                  | 30   | 32  | 96  | 96  | 32                            | 96                               |
| <b>Zero filling factor</b>       | 0  | 2   | 2   | 2   | 2                             | 2                                |
| <b># repetitions</b>             | 1  | 1 per flip angle                                | 1 per flip angle                                | 15  | 6 per flip angle              | 5                                |
| <b>Purpose of scan</b>           | Anatomic image for brain region segmentation | Estimation of pre-contrast T <sub>1</sub> and k | Estimation of pre-contrast T <sub>1</sub> and k | Estimation of SSS signals<br>Estimation of K <sup>trans</sup> | Estimation of PS <sub>w</sub> | Estimation of K <sup>trans</sup> |

Figure 1

Total scan time = 63 minutes

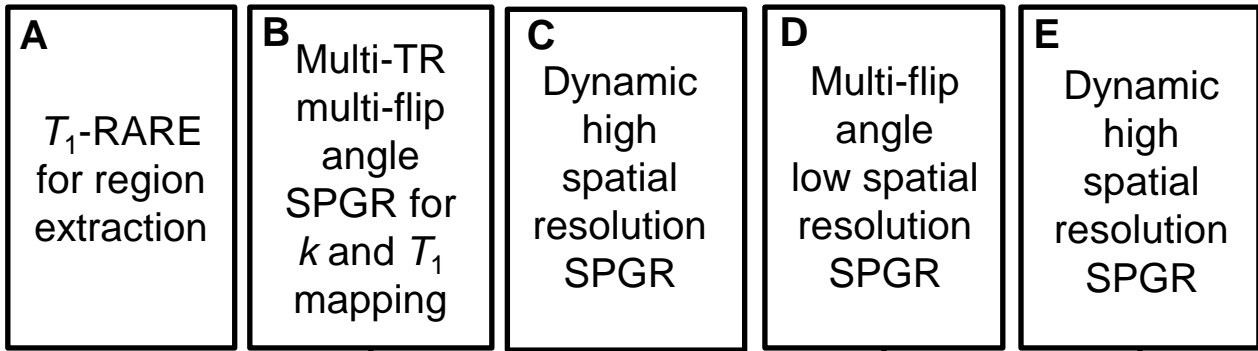
5 min

35.5 min

7.5 min

12.5 min

2.5 min



Inject CA on 6<sup>th</sup> volume

| <u>Long TR</u>   | <u>Short TR</u>                                     |
|--|---|
| $\alpha = [5^\circ, 10^\circ, 20^\circ, 30^\circ, 40^\circ, 60^\circ, 80^\circ, 90^\circ]$ | $\alpha = [10^\circ, 20^\circ, 40^\circ, 60^\circ]$ |
| TR: 5000 ms  | TR = 100 ms   |
| TE: 2.1 ms   | TE: 10 gradient echoes ( $\Delta = 2.1$ ms)         |
| matrix: 32 x 32 x 32   | matrix: 64 x 64 x 96                                |
| $n_{\text{rep}} = 1$   | $n_{\text{rep}} = 1$                                |

|  |
|--|
| $\alpha = 60^\circ$                        |
| TR: 20 ms                                  |
| TE: 6 gradient echoes ( $\Delta = 2.1$ ms) |
| matrix: 64 x 64 x 96                       |
| $n_{\text{rep}} = 15$                      |

|   |
|---|
| $\alpha = [30^\circ, 40^\circ, 20^\circ, 10^\circ, 80^\circ]$ |
| TR: 100 ms  |
| TE: 10 gradient echoes ( $\Delta = 2.1$ ms)                   |
| matrix: 32 x 32 x 32  |
| $n_{\text{rep}} = 6$  |

Figure 2

● Measured data  
— Model fit

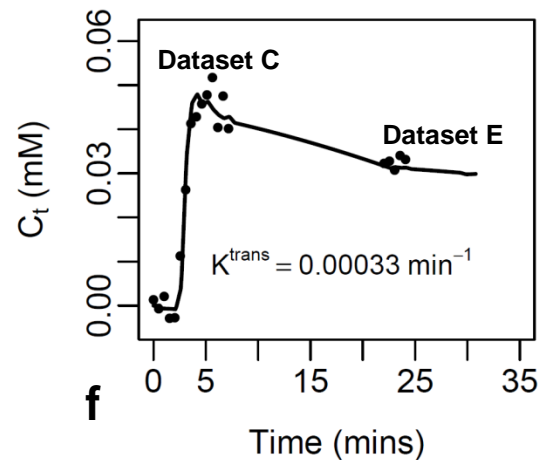
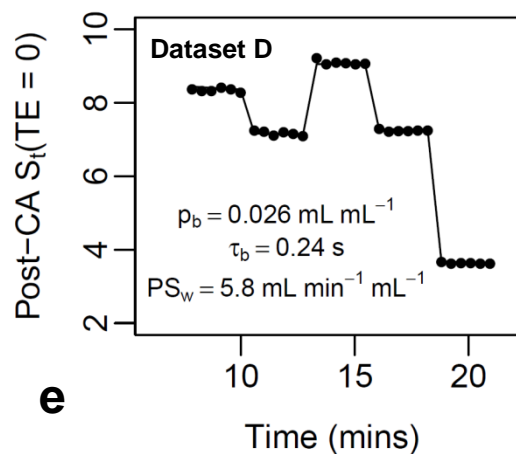
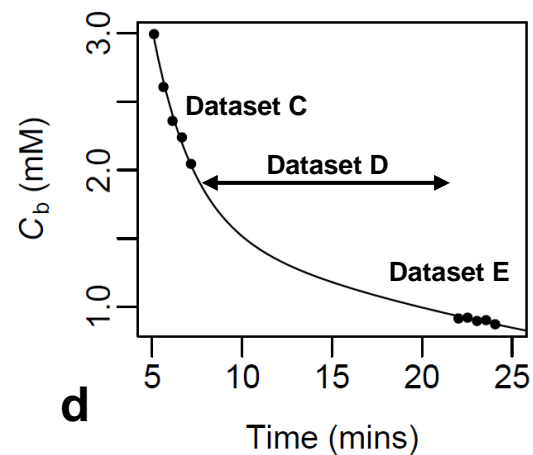
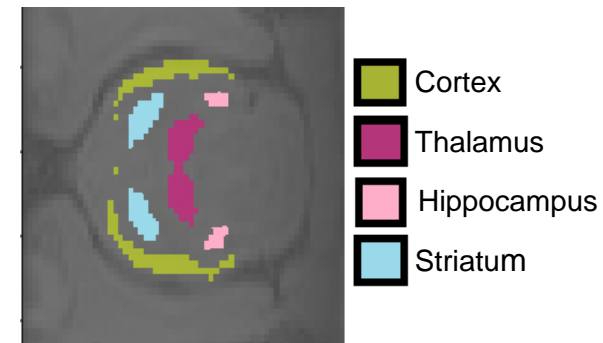
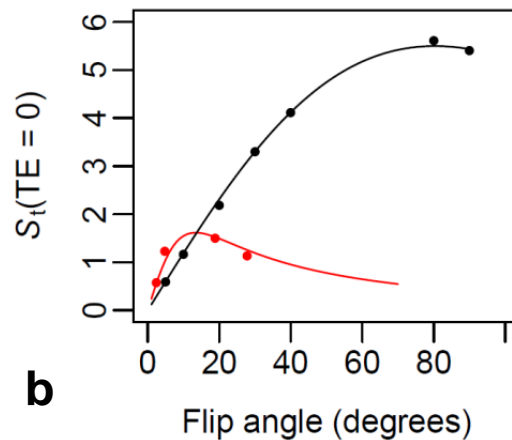
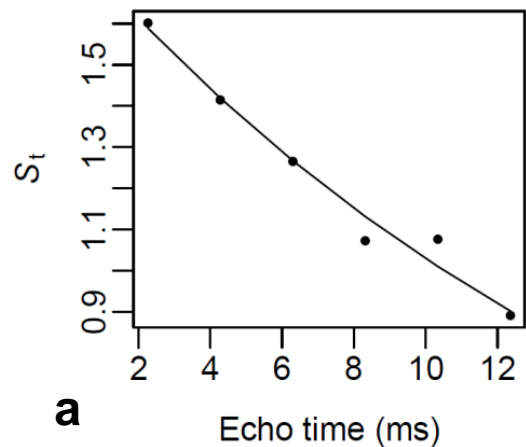


# Figure 3

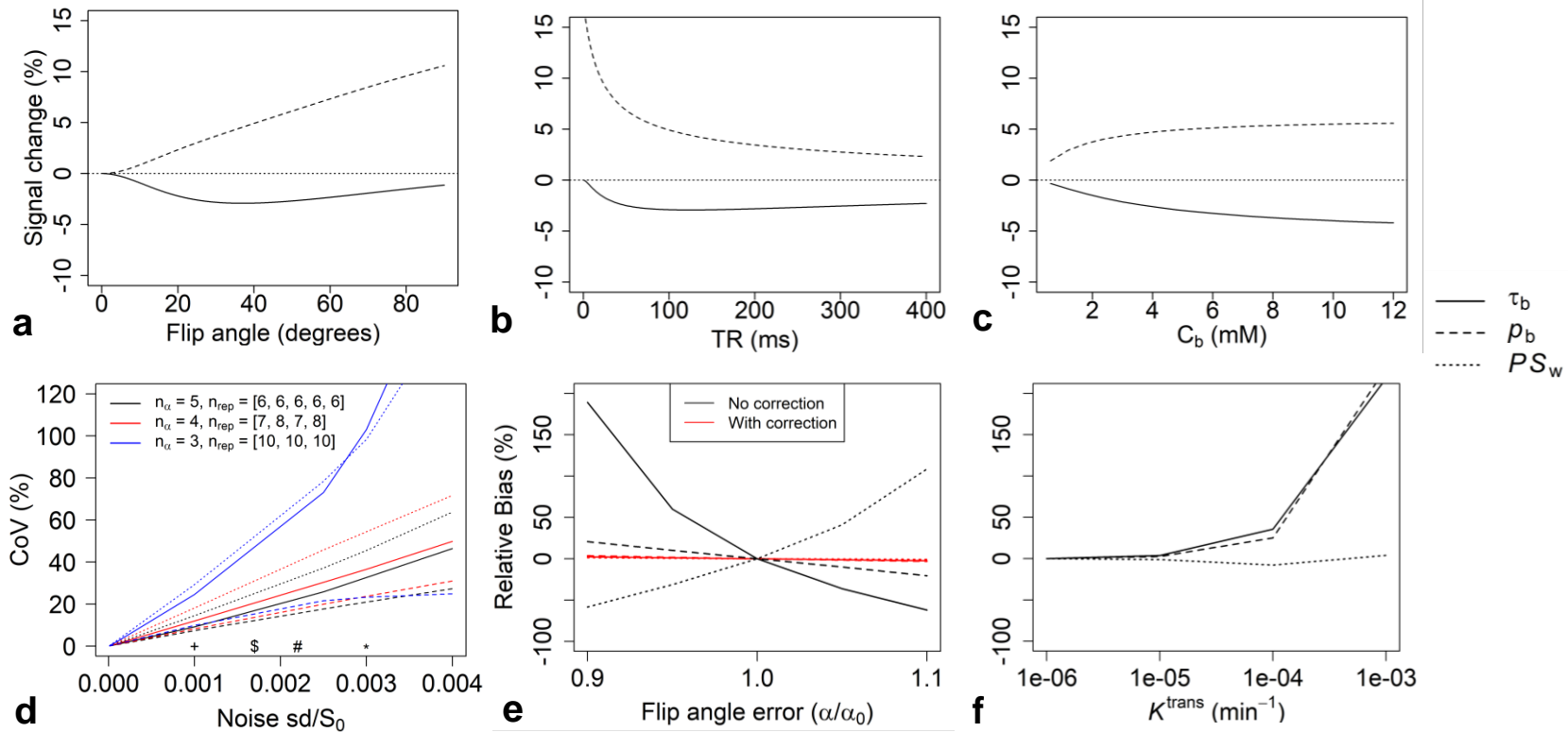
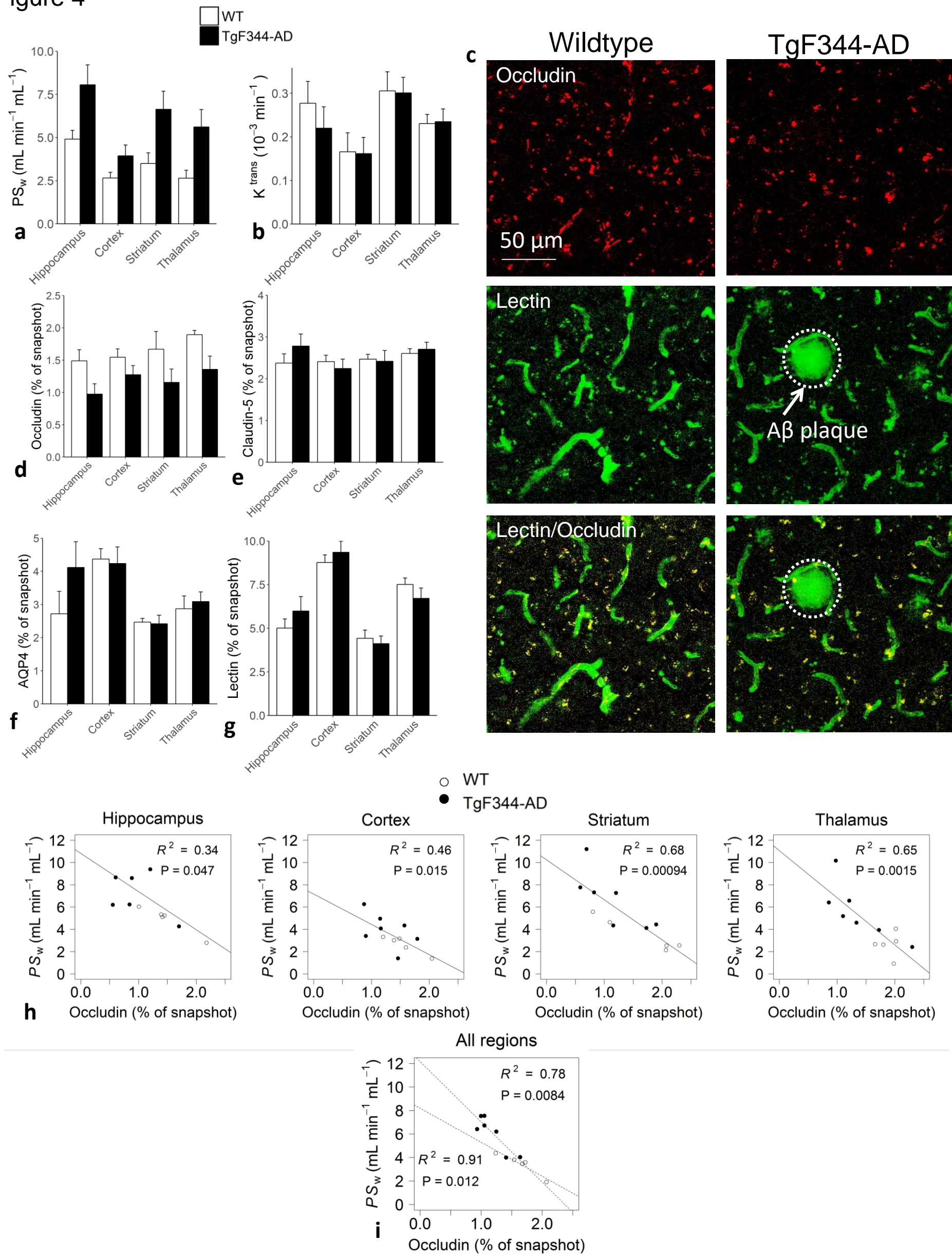


Figure 4





# Figure 5

○ WT  
● TgF344-AD

